AIChE WILEY InterScience DISCOVER SOMETHING GREAT

FLUID MECHANICS AND TRANSPORT PHENOMENA

# Measuring the Velocity Field in Film-Splitting Flows of Newtonian Liquids

**Melisa Z. Becerra, Oldrich Joel Romero, Luis Fernando A. Azevedo, and Marcio S. Carvalho**
Dept. of Mechanical Engineering, Pontificia Universidade Catolica do Rio de Janeiro,
Rua Marques de Sao Vicente 225, Gavea, Rio de Janeiro, RJ, 22453-900, Brazil

*DOI 10.1002/aic.11051*
*Published online December 13, 2006 in Wiley InterScience (www.interscience.wiley.com).*

*Rigorous mathematical analysis of viscous free surface flows and comprehensive experimental analysis have been used to develop coating technology in the last 30 years. Theoretical analysis usually require advanced numerical methods to solve the mass and momentum-conservation equations coupled with the appropriate boundary conditions for flows with liquid-gas interfaces. Experimental analysis usually requires pilot plant trials and bench-top flow visualization experiments to reveal details of the flow inside the coating bead. The first attempts to visualize a coating flow were limited to displaying the free-surface configuration as a function of the operating parameters. Later, careful experiments were used to visualize streamlines with vortices inside a coating bead for different coating processes. Streamline visualization were crucial on enhancing the fundamental understanding of different coating flows. However, the application of quantitative methods capable of providing instantaneous measurements of the velocity field inside a coating bead is still rare. Velocity measurements in coating flows are extremely challenging because of the small scale, and the presence of liquid-air interfaces. In this work, the particle-image velocimetry (PIV) technique was used to study the flow between a rotating roll and a stationary plate, a prototype forward roll coating flow. Theoretical predictions of the same flow were obtained by solving the Navier-Stokes equations with the appropriate boundary conditions for free-surface flows. The velocity and the rate of deformation at each point were measured at different operating parameters. Some of the results were compared with the theoretical predictions.* © 2006 American Institute of Chemical Engineers *AIChE J,* 53: 281–289, 2007

*Keywords: roll coating, free surface, particle-image velocimetry, finite-element method*

## Introduction

Many different products are manufactured by depositing a thin liquid layer onto a moving substrate and, subsequently, solidifying it. Examples of products include premium papers, magnetic tapes and disks, printing materials, photosensitive coatings, membranes, films used in different types of displays, microelectronics circuits and many others.

The region where the liquid first comes into contact with the substrate is called the *coating bead*. It is usually bounded by two gas-liquid interfaces, or menisci, the solid walls of the coating applicator and the moving substrate. The competition among viscous, capillary and pressure forces, and in some cases inertial and elastic forces, sets the range of operating parameters at which the viscous free surface flow can be two-dimensional (2-D), and steady — the conditions prerequisite for uniform coating.

Coating technology remained an art until the 1940's. Since then, rigorous mathematical analysis of viscous free surface flows started to be used to gain basic understanding of coating flows. Today, both industrial and academic coating flow

Correspondence concerning this article should be addressed to M. S. Carvalho at msc@mec.puc-rio.br.

research are based on comprehensive theoretical and experimental analysis.

Theoretical analysis usually require advanced numerical methods to solve the mass and momentum conservation equations coupled with the appropriate boundary conditions for flows with gas-liquid interfaces. Christodoulou et al.[1] review the different methods used to analyze free surface flows, and their application to coating technology development. Most of the theoretical analysis can provide details and insights into the physics that control the two-dimensional (2-D) flow in successful coating operations, stability limits of the flow states and, ultimately, stability limit maps of the process. However, the available theoretical models for coating flow analysis are not able to precisely describe some essential physical mechanisms, such as dynamic wetting and non-Newtonian behavior. Specially in these cases, it is essential to be able to compare the predicted flow states with experimental measurements of the flow-field in order to validate the simplifying assumptions, and to test the constitutive equations used to describe the mechanical behavior of the flowing liquid.

The first attempts to visualize a coating flow were limited to displaying the free surfaces or meniscii position and configurations, and were not able to resolve details of the flow inside the coating bead. Schweizer[2] was the first to present streamlines with vortices in a coating flow. The pictures showed the flow pattern of two liquids merging on an incline plane and in the region between a slide coating applicator and the moving web. Optical access into the flow was gained through a side transparent window mounted such that it coincided with the side confinement of the flowing liquid. The plane of observation, at which the tracer particles were introduced, was sufficiently far from the side window to avoid edge effects and to guarantee a truly 2-D flow. This technique was improved and applied to many other coating methods, such as slot coating,[3] multilayer slide coating[4] and roll coating.[5]

Flow visualization techniques had a strong contribution on enhancing the fundamental understanding of different coating methods, and have provided many new insights into the process. However, in order to understand the flow in more detail, a quantitative method capable of providing instantaneous measurements of the velocity field inside the coating bead is required. For example, if the instantaneous velocity at each point of the flow is known, the deformation rates to which the liquid is subjected inside the coating bead can be calculated. This information is vital to understand the role of liquid rheology on the process. Velocity measurement in coating flows is a challenging task. The main reasons are the small scales of the flow — the coating bead is usually in the order of 100 $\mu m$ — the presence of the free surfaces, and the relatively high-speed in some cases. Reports of velocity field measurements of coating flows are rare in the literature. Hens[6] used laser-doppler anemometry (LDA) to measure the liquid velocity in the vicinity of the dynamic contact line in a slide coating process. The spacial resolution was claimed to be less than 40 $\mu m$. However, in that work, the velocity information was associated with high-levels of uncertainty related to the spatial positioning of the measuring volume, since one of the laser beams was deflected by the meniscus, whose position and shape depend on operating conditions that were not known *a priori*. Clarke[7] used particle tracking velocimetry (PTV) to obtain the velocity field in a curtain coating flow. The liquid velocity was measured by obtaining the velocity of small bubbles as they travelled along streamlines within the curtain. PTV technique tracks individual particle images in consecutive image frames, and the velocity field is obtained, based on the displacement vector for each matched particle pair. This technique yields low-resolution velocity measurements, and the measured velocity vectors are unevenly distributed throughout the flow.

Another widely used nonintrusive flow measuring technique is particle-image velocimetry (PIV). As in PTV, the flow is seeded with small tracer particles externally illuminated by a planar sheet of pulsating laser light, and the scattered light from the tracer particles is recorded. However, in PIV the velocity vectors are not obtained from the displacement vectors for each individual particle. Rather, the image is divided into small interrogation windows, and an area-averaged displacement vector over each interrogation window is obtained by statistical evaluation of two consecutive images. The spatial resolution of the measured velocity field is a function of the size of the interrogation window and can be quite high. Moreover, the measured velocity vectors are evenly distributed over the flow domain, being obtained at predefined positions. Adrian[8] presents an extensive discussion of several aspects of this technique. Although PIV has been widely used in several applications, to our knowledge, this method has not been applied to coating flows.

In this work, we apply the PIV technique and the numerical solution of the Navier-Stokes equation with the appropriate boundary conditions to describe the free surface to determine, experimentally and theoretically, the velocity field near the downstream free surface of a prototype forward roll coating flow. Roll coating is distinguished by the use of one or more gaps between rotating cylinders to meter and apply a liquid layer to a substrate. The position of the free surface is a strong function of the operating conditions, and a recirculation, attached to the meniscus, is present at low-roll speeds. Above a critical roll speed, the 2-D film splitting flow that occurs in forward roll coating becomes unstable; a 3-D steady flow sets in, resulting in more or less regular stripes in the machine direction, as shown in Figure 1. The stability of the 2-D flow is determined by the competition of the different forces acting on the free surface — capillary, viscous and elastic, in the case of polymeric solutions. For Newtonian liquids, the onset of meniscus nonuniformity is marked by a critical value of the capillary number. Therefore, in order to fully understand this flow stability limit, it is very important to accurately measure the velocity field near the free surface to be able to estimate the


**Figure 1. 3-D periodic flow in a forward roll coating film splitting flow.**

[Color figure can be viewed in the online issue, which is available at www.interscience.wiley.com.]

different forces acting in that region of the flow. In the case of viscoelastic liquids, measuring the instantaneous velocity field near the free surface is even more important, since it will reveal the role of the liquid rheology on the flow pattern, what can be used to validate the different constitutive models used to describe viscoelastic behavior of polymer solutions.

The velocity field near the meniscus is measured at different flow conditions. The results are used to evaluate the deformation rates at each point of the flow. The experimental results were compared to the theoretical predictions obtained by solving the governing equations using Galerkin's/finite-element method.

## Experimental Analysis

### *Description of the test section*

The experiments were conducted in the test section shown in Figure 2. It consisted of a stationary glass plate and a rotating roll. Liquid was picked out of a pan and a liquid bead was formed in the small space between the plate and the roll. A meniscus was formed in the region where the liquid detached from the plate, forming a film of liquid on the roll surface.

The test section was specially designed to allow visualization of the coating bead from two different angles: a frontal view, through the glass plate, and a lateral view through a side glass plate mounted to give optical access to the flow. The front view was used to determine the configuration of the static contact line across the width of the plate and, consequently, the onset of the 3-D configuration of the meniscus. The lateral view was used to visualize the flow pattern and the meniscus configuration, and also to allow the measurement of the velocity field near the free surface by means of the particle-image velocimetry (PIV) technique.

The main component of the test section was the rotating roll. It was a chromed-plated, solid steel cylinder with dimensions of 200 mm $\times$ 400 mm (dia. $\times$ length). The cylinder had one supporting shaft on each side. The shafts were supported by ball bearings attached to a solid steel table. The maximum eccentricity obtained with this assembly while the roll was rotated was of the order of 20 $\mu$m. An electrical motor requipped with a programmable speed control was used to rotate the roll. Two pulleys connected with a synchronized rubber belt were used to drive the steel shaft, providing a transmission ratio of 10:1. The motor speed control and the low-transmission ratio, allowed for a smooth control of the roll angular speed. An encoder was installed at the tip of the steel shaft to measure its angular speed. The stationary plate was formed by a 200 mm $\times$ 400 mm $\times$ 6 mm (height $\times$ width $\times$ thickness), optical quality glass, supported in the vertical position by a Plexiglas frame mounted on precision linear stages. The roll-to-plate gap was established by sliding the glass plate horizontally. Pieces of stainless steel shim stock of known thickness were introduced between the roll surface and the glass plate to set the desired gap for a particular experiment. A side glass plate was glued to one of the lateral edges of the glass plate, as shown in Figure 2. This plate was used to facilitate the observation of tracer particles in the coating film by the digital camera during the velocity measurements, as will be explained shortly. The operating parameters that were controlled during the experiments were the gap between the roll and the stationary plate $H_0$, the tangential roll speed $V$, and the viscosity of the Newtonian liquid $\mu$. The relevant dimensionless parameters that govern the problem are:

- Gap-to-roll radius ratio $G \equiv \frac{H_0}{R}$,
- Capillary number: $Ca \equiv \frac{\mu V}{\sigma}$, $\sigma$ is the surface tension of the liquid.

In the experiments presented in this work, the gap was kept approximately constant at $H_0 = 900\ \mu m$ (measured roll run-out of 20 $\mu m$), that is $\frac{H_0}{R} = 9 \times 10^{-3} \pm 0.5 \times 10^{-3}$.

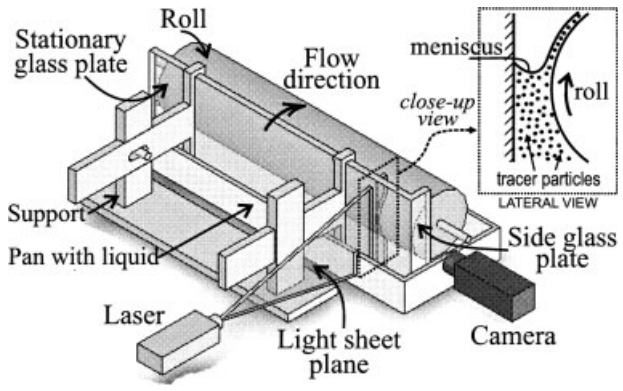


**Figure 2. Main features of the experimental roll plate apparatus.**

A lateral view of the meniscus is also shown in the top right corner of the figure.

## Velocity Measurements

The velocity field between the moving roll and the stationary plate in the neighborhood of the free surface was measured for different flow conditions using the particle-image velocimetry technique. In this technique a pulsed laser sheet illuminates small tracer particles previously distributed in the fluid. A digital camera mounted orthogonally to the laser sheet records the position of the tracer particles at two close instants. A synchronization circuit coordinates the laser pulse with the image capturing system, so that the two images are registered in consecutive frames. The particle displacements are determined by analyzing small subregions of the image (the interrogation windows), and cross-correlating the image intensity distribution of the two frames. This process yields the mean-particle displacement for each interrogation window. The instantaneous velocity field is obtained by dividing the instantaneous displacement field by the time interval between laser pulses, and by the magnification factor of the optical setup.

In this experiments, a PIV system manufactured by TSI, Inc. was utilized. This system employed a pair of integrated New Wave, frequency-doubled, Nd-YAG lasers capable of delivering up to 120 mJ of energy per pulse, at 15 Hz. The digital camera employed was a PIVCAM model 10-30 with a resolution of 1,000 pixels $\times$ 1,000 pixels using a lens that yielded a magnification of 2.4 X.

This camera was mounted on a *x-y-z* coordinate table. The field of view was a square with sides of approximately 6 mm. Synchronization between the laser and the camera was controlled by a TSI model 60006 unit. The particle images were captured and processed by the Insight software (cross-correlation-based algorithm) developed by TSI, Inc.

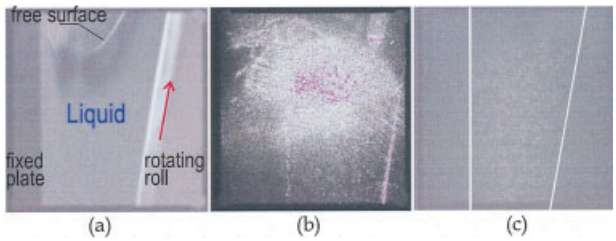


**Figure 3. Example of images obtained through the side view (a) without tracer particle, (b) with tracer particles (reflection comes from the free surface), and (c) with fluorescent tracer particles and optical filter undesired reflections are eliminated.**

[Color figure can be viewed in the online issue, which is available at www.interscience.wiley.com.]

The major difficulty in applying the PIV technique to measure free surface flows in the vicinity of the free surface, arises from the light reflections originated at the gas-liquid interface. The light reflected at the gas-liquid interface is normally much more intense than the light scattered by the tracer particles, what precludes the registration of their images on the recording media. The proposed solution for this problem was to use a combination of fluorescent tracer particles and optical filters to avoid the undesired reflections. The tracer particles chosen were polymer microspheres with a mean diameter of 3 $\mu m$, and impregnated with rodhamine dye. These particles scatter red light at a wavelength of approximately 590 nm when illuminated by the green laser light coming from the YAG laser ($\sim$532 nm). An optical filter with a cutoff wavelength of 570 nm was placed in front of the camera lens blocking most of the green light reflect by the free surface, thereby making the tracer particles clearly visible. Figure 3 presents an example of the improvement in particle image obtained with the technique described. For reference purposes, Figure 3a presents an image of the flow region obtained with room illumination and no tracer particles present. The image shows the vertical stationary glass plate, the rotating roll and the curved free surface. In Figure 3b the image was obtained with regular (not fluorescent) tracer particles, and with the YAG laser sheet illumination. It can be seen in the figure that reflection from the free surface masks all tracer particles. No meaningful velocity data can be obtained from a picture like this. In Figure 3c the fluorescent tracer particles are clearly visible after the light reflected by the free surface was blocked by the optical filter. In this figure, the shape of the free surface becomes evident by the position of the tracer particles. The particle image pairs were processed to determine the velocity field using an interrogation window with 32 pixels $\times$ 32 pixels, which corresponds to 190 $\mu$m $\times$ 190 $\mu$m in the actual flow. Calibrating experiments previously conducted with a solid-body rotation apparatus, indicated that the experimental accuracy of the PIV system used here is of the order of $\pm 1\%$ (see[9]).

Although the process conditions (gap and roll speed) were held constant during each measurement procedure, the flow oscillated periodically due to the small variations of the actual radius along the circumference of the roll about its specified value of $R = 100$ mm. We estimated this variation, generally referred to as roll run-out, as being approximately 20 $\mu$m. Because of the small clearance between the rotating roll and the plate, any small variation of the roll radius caused an appreciable variation of the gap. Consequently, the flow is unsteady, and the meniscus position oscillates periodically. Figure 4 shows the instantaneous velocity fields measured at $H_0/R = 9 \times 10^{-3}$ and $Ca = 0.17$ at the position of minimum and maximum roll-to-plate gap. The motion of the meniscus is clear, the position of the free surface varies from $Y_{\text{men}} = 24.6$ mm to $Y_{\text{men}} = 25.6$ mm — oscillation of approximately 1 mm.

In order to report average values for the velocity field, a time-average of the velocity at each measured position was calculated. The sampling time was always larger than six revolutions of the roll, what corresponded to 200 velocity fields forming a typical sample. The averaged velocity field at the process conditions shown in Figure 4 is presented in Figure 5. It is important to notice that the time-average introduces uncertainty on the location of the meniscus. Because the flow domain is defined by the presence of tracer particles, the meniscus position associated with the time-averaged velocity field is the same as the position associated with the flow of maximum gap, approximately $Y_{\text{men}} = 25.6$ mm, not the average of all the measured meniscus configurations. Away from the free surface, at which individual interrogation volumes contain tracer particles at all times, the time-average process represents better the flow. The vortex center position during one revolution of the roll varies from $Y_{\text{vc}} \approx 22$ mm to $Y_{\text{vc}} \approx 23$ mm, whereas it is located at $Y_{\text{vc}} \approx 22.4$ mm on the time-averaged velocity field.

## Liquid Properties

The transparent liquid used in the experiments was a Newtonian solution of low-molecular-weight polymer (PEG, polyethylene glycol, molecular weight 6,000 g/mol) in water. The concentration of the PEG was fixed at 30% by weight, which yielded a constant viscosity of approximately 30 cP, measured using a rotational rheometer (ACER, Rheometrics, Inc.), with a cone-and-plane fixture. The density of the solution was $\rho = 1047\ kg/m^3$, and the surface tension was $\sigma = 52 \times 10^{-3}\ N/m$.

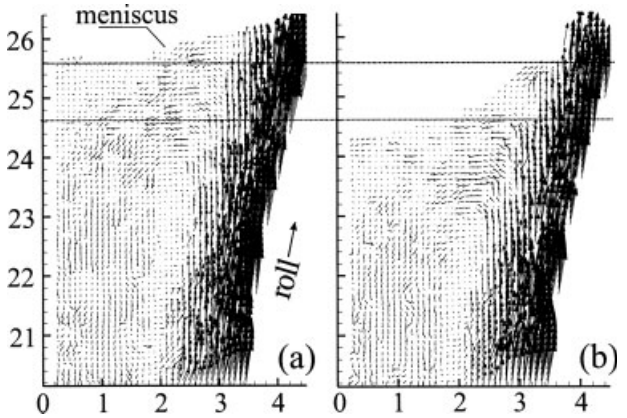


**Figure 4. Velocity vectors at two extreme positions at mean gap of $H_0/R = 9 \times 10^{-3}$ and $Ca = 0.17$ showing the meniscus oscillation as the gap varies due to the roll runout.**

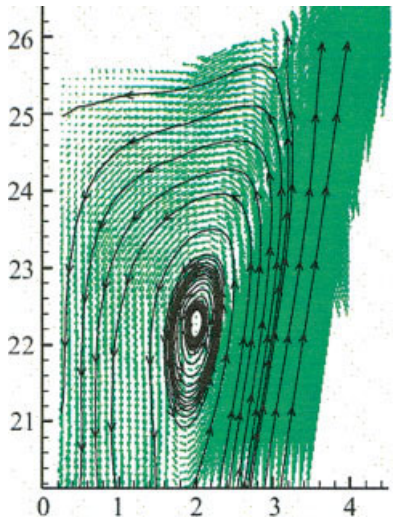


**Figure 5. Average velocity field at *Ca* = 0.17.**

This was obtained postprocessing 200 images similar to the ones presented in Figure 4. [Color figure can be viewed in the online issue, which is available at www.interscience.wiley.com.]

## Theoretical Analysis

Although the flow in the experiments was transient (periodic) due to the roll run-out, the theoretical description of the flow in the coating bead was done using the complete 2-D, steady-state mass and momentum conservation equations for a Newtonian liquid. Modeling the transient flow would require information on the hysteresis behavior of the contact angle between the liquid-air interface and the glass plate. The goal of the theoretical analysis was to determine the effect of the different operating parameters, for example, gap, roll speed and contact angle, on the steady flow near the meniscus. The predicted velocity field at different flow conditions was compared to the time-average values of the measured velocity at each point in the flow. At low-Reynolds number flows, as the ones analyzed here, time-average velocity fields should approach the corresponding steady-state values.

The flow domain where the governing equations are solved was restricted to the cross-section plane close to the downstream free surface, as sketched in Figure 6. The gap between the rotating roll and the fixed plate was set to $H_0 = 900\ \mu m$; also, the roll radius was the same as that used in the experiments, that is, $R = 100\ mm$. The synthetic inflow boundary was placed at $25H_0$ upstream of the plane of minimum distance between the roll and the plate. The outflow plane was placed $50H_0$ downstream of the same plane.

## Governing Equations and Boundary Conditions

The velocity $\mathbf{v}$ and pressure $\mathbf{p}$ fields for 2-D Navier-Stokes flows are governed by the continuity- and momentum-conservation equations

$$\nabla \cdot \mathbf{v} = 0, \quad \rho(\mathbf{v} \cdot \nabla \mathbf{v}) = \nabla \cdot [-p\mathbf{I} + \mu(\nabla \mathbf{v} + \nabla \mathbf{v}^{\mathrm{T}})] \tag{1}$$

where $\mu$ is the liquid viscosity.

The boundaries of the flow domain are labeled in Figure 6, and the corresponding boundary conditions are the following:

1. *Inflow:* Imposed pressure as a traction condition

$$p = P_0 \tag{2}$$

2. *Plate:* No-slip, no-penetration

$$\mathbf{v} = 0 \tag{3}$$

3. *Static contact line:* The contact line is free to move with a prescribed contact angle

$$\mathbf{n}_w \cdot \mathbf{n}_{fs} = \cos(\theta) \tag{4}$$

$\theta$ is the angle between the free surface unit normal vector $\mathbf{n}_{fs}$ and the plate surface unit normal vector $\mathbf{n}_w$. A range of contact angles of $30^\circ < \theta < 90^\circ$ was explored in the numerical solutions

4. ***Free surface:*** Force balance and kinematic condition

$$\mathbf{n}_{fs} \cdot \mathbf{T} = \sigma \frac{d\mathbf{t}_{fs}}{ds} - \mathbf{n}_{fs}\, p_{\mathrm{amb}} \tag{5}$$

$$\mathbf{n}_{fs} \cdot \mathbf{v} = 0 \tag{6}$$

$\mathbf{t}_{fs}$ and $\mathbf{n}_{fs}$ are the local unit tangent and unit normal to the free surface, $\mathbf{T}$ is the liquid stress tensor, $\sigma$ is the liquid surface tension and $p_{\mathrm{amb}}$ is the ambient pressure

5. *Outflow:* Fully developed flow

$$\mathbf{n} \cdot \nabla \mathbf{v} = 0 \tag{7}$$

$\mathbf{n} \cdot \bigtriangledown$ is the directional derivative perpendicular to the outflow plane.

6. ***Moving roll:*** No-slip, no-penetration

$$\mathbf{v} = \mathbf{V} \tag{8}$$

## Solution Method

Because of the free surface, the flow domain at each set of parameter values is unknown *a priori*. To solve the free boundary problem by standard techniques for boundary value problems, the set of differential equations and boundary conditions posed in the unknown domain $\Omega$ (with boundaries $\Gamma$) has to be transformed to an equivalent set defined in a known reference domain $\Omega_0$ (with boundaries $\Gamma_0$). This can be done with a map-

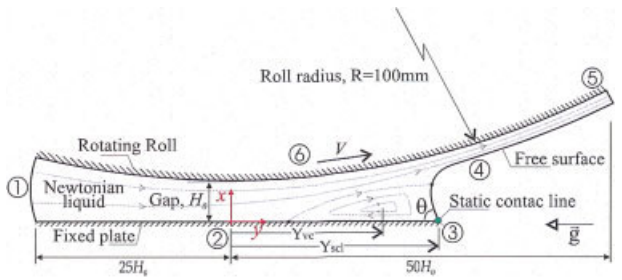


**Figure 6. Flow domain with boundary conditions used for the theoretical analysis.**

[Color figure can be viewed in the online issue, which is available at www.interscience.wiley.com.]

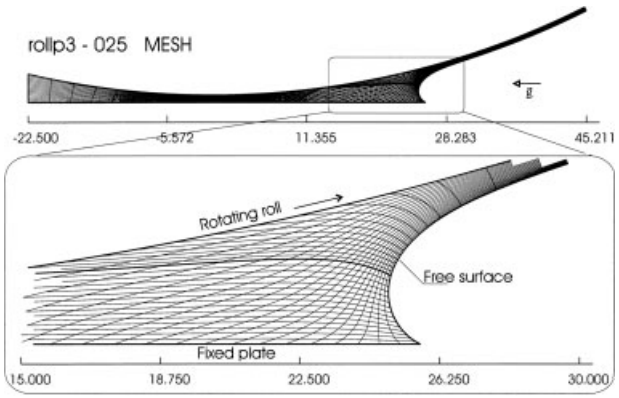


**Figure 7. Typical mesh in the full domain and detail close the downstream meniscus.**

ping $\mathbf{x} = \mathbf{x}(\xi)$ that connects the two domains.[10] The unknown physical domain is parameterized by the position vector $\mathbf{x}$, and the reference domain by $\xi$. The inverse of the mapping, $\xi = \xi(\mathbf{x})$, that minimizes the functional is governed by a pair of elliptic-differential equations.

$$\nabla \cdot (D_\xi \nabla \xi) = 0, \quad \nabla \cdot (D_\eta \nabla \eta) = 0 \tag{9}$$

Here, $D_\xi$ and $D\eta$ are diffusion-like coefficients used to control gradients in coordinate potentials, and thereby the spacing between curves of constant $\xi$ on the one hand and of constant $\eta$ on the other that make up the sides of the elements that were employed; they were quadrilateral elements. Boundary conditions were needed in order to solve the second-order partial differential equations, given by Eq. 9. The solid walls and synthetic inlet and outlet planes were described by functions of the coordinates, and along them stretching functions were used to distribute the terminii of the coordinate curves selected to serve as element sides. The free boundary (gas-liquid interface) required imposing the kinematic condition, viz. Eq. 6.

The set of differential equations that describe the conservation of mass and momentum in Eq. 1, and define the mapping between the physical and reference domain, Eq. 9, together with the appropriate boundary conditions, were all solved on the reference domain by the Galerkin/finite element method.

The position of the flow domain $\mathbf{x}$ and velocity $\mathbf{v}$ fields are represented by Lagrangian biquadratic basis functions, while the pressure field $p$, by linear discontinuous basis functions. The mesh generation equations and the momentum equation are weighted with Lagrangian biquadratic basis functions, and the continuity equation with linear-discontinuous basis functions.

The set of nonlinear algebraic equations that arises from applying the method of weighted residuals and the variables representation in terms of basis functions is solved by Newton's method with analytical Jacobian, and first-order arclength continuation,[11] and a bordering algorithm[12] or block elimination. The tolerance of the $L_2$-norm of the residual vector and the last Newton update for each solution was set to $10^{-6}$.

The domain was divided into 1,100 graded quadrilateral elements with 21,544 unknowns. Test showed that using more elements produced changes in the values of the coefficients no greater than 1%. Figure 7 shows the tessellation of the full domain and the detail near the free surface of the mesh used in this work.

## Results

The presentation of the results starts with the observations of the contact line made through the stationary glass plate. The goal of the observations was to detect the onset ribbing for a fixed gap, as the roll speed (that is, the capillary number) was raised. A sequence of images of the contact line for increasing values of the capillary number is presented in Figure 8. At low-capillary numbers, represented in Figure 8a and b, the flow is 2-D, and the position of the contact line does not vary along the transverse direction. The contact line appears as a straight line in the figures. At a capillary number of approximately $Ca \approx 0.54$, the contact line becomes wavy as an indication of a periodic and 3-D meniscus. Figure 8c was taken at a slightly higher value of the capillary number, namely $Ca \approx 0.57$. The image in Figure 8d, taken at $Ca \approx 0.83$, shows that the amplitude of the variation of the position of the contact line increases as the capillary number is raised above the critical value.

The effect of the capillary number on the time-average velocity field is shown in Figure 9. The average velocity field, measured in a vertical plane, is shown in Figures 9a and b, for values of the capillary number below the critical value for onset of ribbing, a condition at which the flow is 2-D. As the capillary number is increased beyond the critical value of $Ca \approx 0.54$, the flow is 3-D. The flow fields measured above the critical condition are shown in Figures 9c and d. For these cases, the laser light sheet was positioned at a meniscus valley. The flow fields shown represent, therefore, the components of the flow in the vertical plane. A general observation of Figures 9a–d reveals that at low-values of the capillary number the flow displays a large zone of recirculating flow, extending between the two solid walls and up to the free surface. A narrow region of up-moving flow is located at the roll surface. As expected, the highest speeds are found near the roll surface. As the capillary number is raised by increasing the roll speed, the recirculating zone decreases in size, being pushed toward the fixed vertical plate. The zone of recirculating flow almost vanishes at the highest value of the capillary number investigated and shown in Figure 9d.

The variation of the position of the meniscus $Y_{\text{men}}$, and the vortex center $Y_{\text{vc}}$ with the roll speed, represented in terms of the capillary number, of the time-averaged flows is shown in

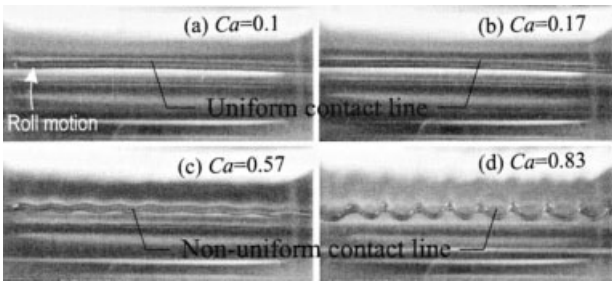


**Figure 8. Frontal view of the contact line through the glass plate as a function of the capillary number at $H_0/R = 9 \times 10^{-3}$.**

The meniscus becomes unstable at $Ca \approx 0.54$.

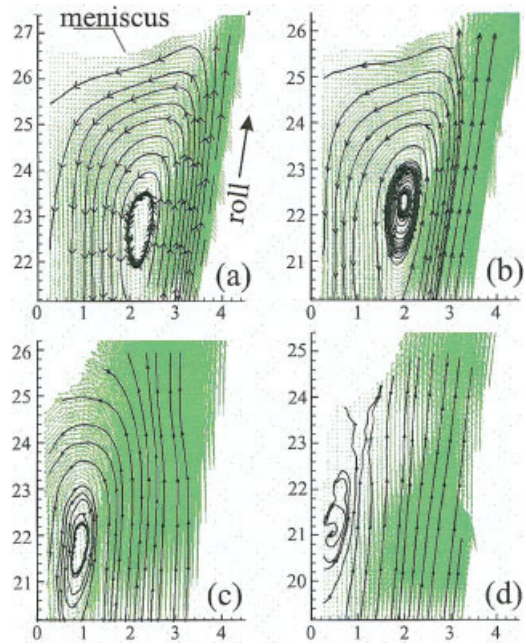


**Figure 9. Lateral view of the flow showing the average velocity fields at different capillary numbers: (a) $Ca = 0.1$, (b) $Ca = 0.17$, (c) $Ca = 0.57$, (d) $Ca = 0.83$ and $H_0/R = 9 \times 10^{-3}$.**

Horizontal and vertical axes values are in mm. [Color figure can be viewed in the online issue, which is available at www.interscience.wiley.com.]

Figure 10. The coordinates are measured from the position of the plane of minimum distance between the roll and the plate. Above the critical capillary number at the onset of the three-dimensional meniscus configuration, the meniscus position is represented by the coordinate of the lower portion (valleys) of the 3-D contact line. The contact line and the vortex center move toward the plane of minimum distance between the roll and plate as the capillary number is raised.

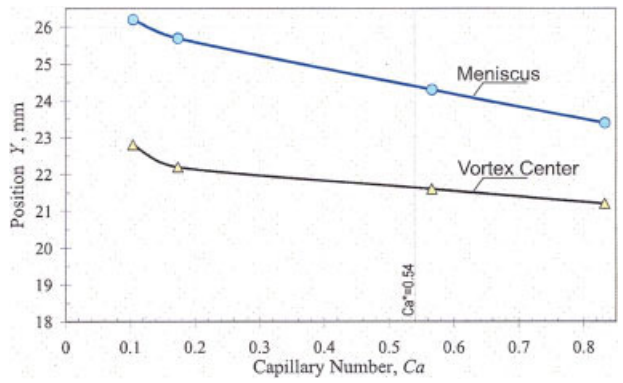


**Figure 10. Meniscus and vortex center position as a function of the Capillary measured at $H_0/R = 9 \times 10^{-3}$.**

In this configuration $Ca^* = 0.54$, is the critical capillary number at the onset of the 3-D flow. [Color figure can be viewed in the online issue, which is available at www.interscience.wiley.com.]

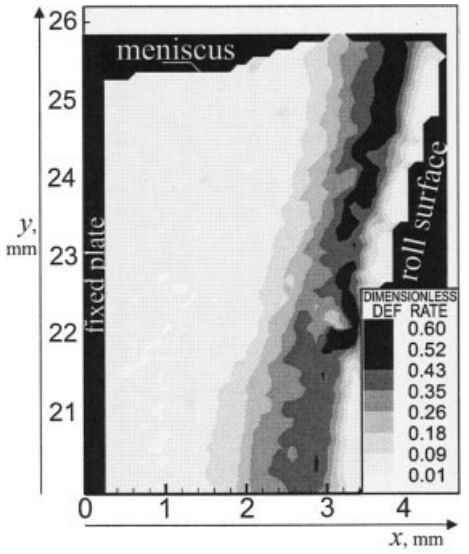


**Figure 11. Deformation rate $\dot{\gamma}$ defined by Eq.10, based on the velocity-field measurements at capillary number $Ca = 0.17$.**

This condition corresponds to the velocity field presented in Figure 9b.

The deformation rate field can be evaluated based on the measured time-average velocity field as

$$\dot{\gamma} = \sqrt{\frac{1}{2} tr\, \dot{\gamma}^2} = \sqrt{2\left(\frac{\partial u}{\partial x}\right)^2 + 2\left(\frac{\partial v}{\partial y}\right)^2 + \left(\frac{\partial v}{\partial x} + \frac{\partial u}{\partial y}\right)^2} \qquad (10)$$

where $\dot{\gamma} \equiv \nabla \mathbf{v} + \nabla \mathbf{v}^{\mathbf{T}}$ is the rate of deformation tensor.

The computed deformation rate, in units of roll speed over gap $V/H_0$, at $H_0/R = 9 \times 10^{-3}$ and $Ca = 0.17$, is shown in Figure 11. The deformation rate could not be evaluated too close to the roll surface due to experimental difficulties associated with measuring velocity vector close to a moving solid surface. As expected, the deformation rate inside the recircula-

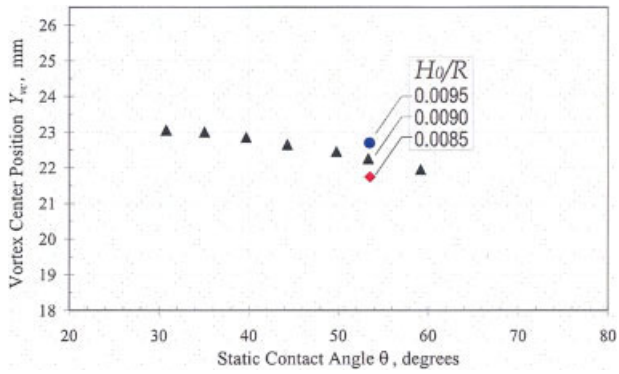


**Figure 12. Theoretical predictions of the vortex center position as a function of the contact angle at capillary number $Ca = 0.17$, and three different gap-to-roll ratio $H_0/R$.**

[Color figure can be viewed in the online issue, which is available at www.interscience.wiley.com.]

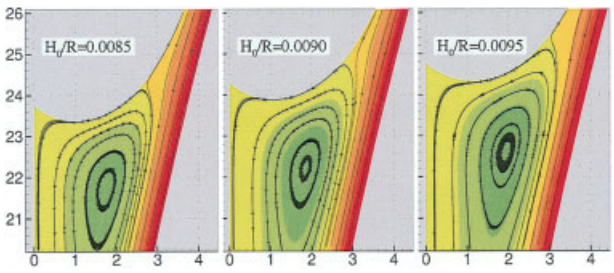


**Figure 13. Predicted streamlines at three different gap-to-roll ratio $H_0/R$ and static contact angle $\theta = 54^\circ$.**

[Color figure can be viewed in the online issue, which is available at www.interscience.wiley.com.]

tion region is very small. The region of the highest deformation rates is located near the roll surface and under the meniscus, and it is approximately $\dot{\gamma} = 0.6\, V/H_0$. This information is crucial for determining the actual viscosity of shear sensitive liquids near the free surface.

The comparison of the measured time-average velocity fields with the theoretical predictions of steady flows is presented next. As mentioned before, the comparison was done based on the assumption that at low-Reynolds numbers, the time-average velocity should approach the corresponding steady state value. However, the situation analyzed in this work is even more complex because of the contact angle hysteresis. As the meniscus oscillates due to the roll run-out, the contact angle at each instant also oscillates between the receding and advancing contact angle values. The relation between equilibrium static contact angles (used in the theoretical predictions), and time-average dynamic contact angles at the contact line is unknown *a priori*.

The predicted vortex center position is a function of the imposed contact angle and roll-plate distance, as shown in Figure 12. The figure shows the position of the center of the recirculation $Y_{vc}$ as a function of the imposed contact angle at $H_0/R = 9 \times 10^{-3}$ and $H_0/R = 9.5 \times 10^{-3}$, $H_0/R = 8.5 \times 10^{-3}$; and $Ca = 0.17$. At a fixed gap, as the contact angle rises, the meniscus curvature and the pressure jump across the interface falls and, consequently, the meniscus and the recirculation center move upstream. The same effect is observed as the gap between the roll and the plate falls. The streamlines of the steady flows at an imposed contact angle of $\theta = 54^\circ$ as a function of the gap is presented in Figure 13. The effect of the imposed contact angle on the streamlines

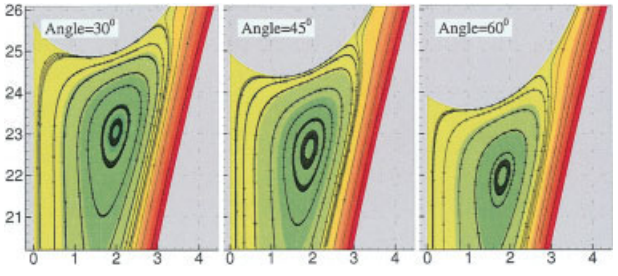


**Figure 14. Predicted streamlines at three different static contact angles and gap-to-roll ratio.**

[Color figure can be viewed in the online issue, which is available at www.interscience.wiley.com.]

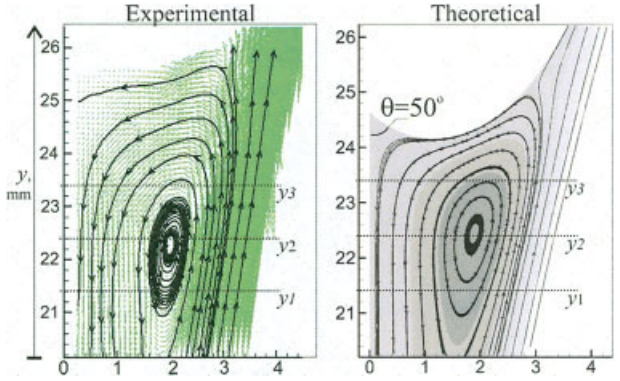


**Figure 15. Predicted and measured flow field at $Ca = 0.17$ and $H_0/R = 9 \times 10^{-3}$.**

Both results show a large recirculation attached to the free surface. [Color figure can be viewed in the online issue, which is available at www.interscience.wiley.com.]

at $H_0/R = 9 \times 10^{-3}$ are shown in Figure 14. At $\theta = 30^\circ$, the vortex center is located at $y \approx 23.1$ *mm*, where as at $\theta = 60^\circ$, it is located at $y \approx 22$ *mm*. The comparison of the steady-state solution with the measured time-averaged velocity field was done at an imposed contact angle that yielded the same vortex center position measured in the experiments, that is, $\theta = 50^\circ$.

The predicted and measured streamlines at $H_0/R = 9 \times 10^{-3}$ and $Ca = 0.17$ are shown in Figure 15. Except for the meniscus configuration, the agreement on the flow pattern is good. As explained before, the time average used to represent the transient flow fields introduces uncertainties on the location of the free surface. The measured and predicted vertical-velocity profiles are compared at three different vertical positions: $y = 21.4$ *mm* (upstream of the vortex center), $y = 22.4$ *mm* (at the vortex center), and $y = 23.4$ *mm* (downstream of the vortexcenter) — see Figure 16. As can be seen in the figure, the agreement is very good. The largest discrepancies are observed near the roll surface.

The predicted deformation rate field is presented in Figure 17. The measured deformation rate evaluated from the measured velocity field is also show for comparison purposes. Inside the recirculation region, the flow is weak and the deformation rate is small. The maximum deformation rate region is located near the roll surface, under the free surface, as in the experimental measurements. The qualitative values of the measured deformation rate agree well with the theoretical prediction.

## Summary

Particle-image velocimetry technique was applied to measure the velocity field near the free surface in a film splitting flow of Newtonian Liquid. The major challenge in measuring the velocity field near the free surface is the light reflection originated at the curved gas-liquid interface, which is normally much more intense than the light scattered by the tracer particles dispersed in the flowing liquid.

The combination of fluorescent particles and an optical filter placed in front of the camera to block most of the light reflected by the free surface was used to eliminate the undesired reflections. The roll run-out caused an oscillation of the position of the free surface, and the static contact angle

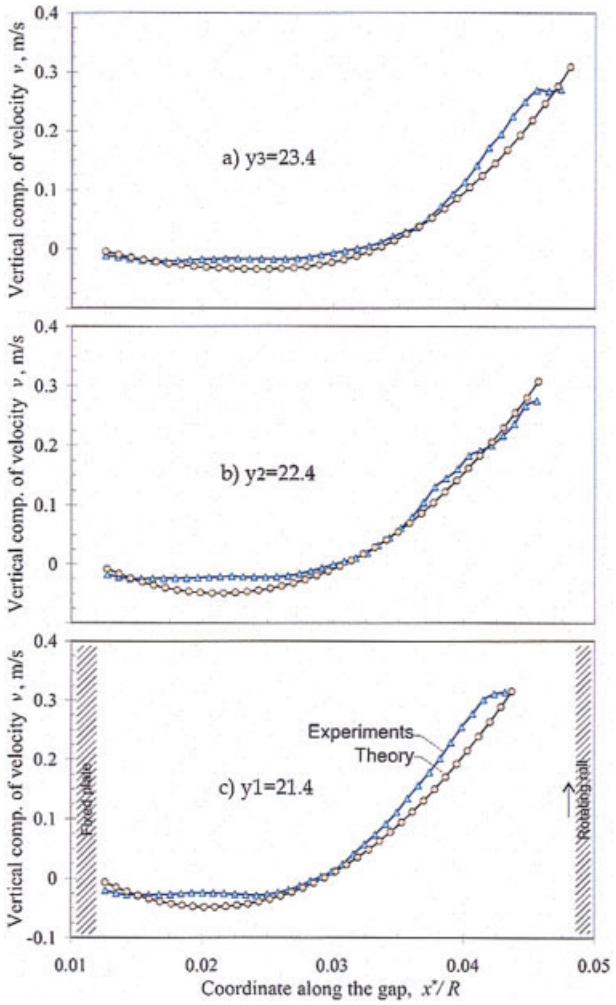


**Figure 16. Comparisons of the vertical velocity across the gap at $y = y_3 = 23.4mm$, $y = y_2 = 22.4mm$ and $y = y_1 = 21.4mm$, obtained by experiments and theory at capillary number $Ca = 0.17$ and $H_0/R = 9 \times 10^{-3}$.**

[Color figure can be viewed in the online issue, which is available at www.interscience.wiley.com.]

between the meniscus and the stationary plate. In order to compare the measurements with steady state numerical solution of the Navier-Stokes equation, with the appropriate boundary conditions to describe the free surface, time-average of the velocity at each measured position was calculated. The sampling time was always larger than six revolutions of the roll, what corresponded to 200 fields forming a typical sample. The evaluation of the time-average introduces uncertainty on the location of the meniscus, but the agreement of the predicted and measured velocity profiles at different positions along the plate, far enough from the free surface, was very good.

The method proposed here to eliminate reflection from the free surface in combination with the PIV technique may be used to measure the velocity field in other coating methods. The quantitative knowledge of the velocity field inside the coating bead would certainly contribute to enhance the fundamental understanding of the process.

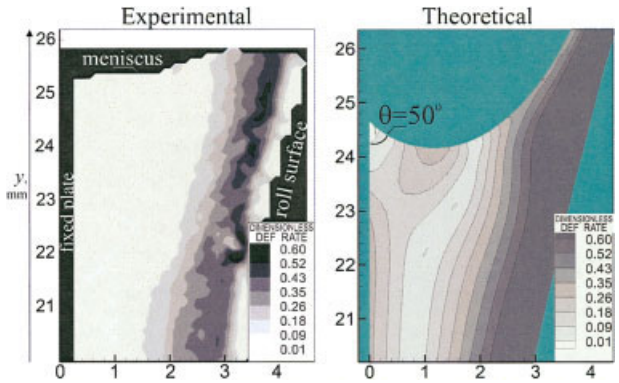


**Figure 17. Comparisons of deformation rate $\dot{\gamma}$ obtained by experiments and theory at capillary number $Ca = 0.17$ and $H_0/R = 9 \times 10^{-3}$.**

[Color figure can be viewed in the online issue, which is available at www.interscience.wiley.com.]

## Literature Cited


1. Christodoulou KN, Kistler SF, Schunk PR. Advances in Computational methods for Free Surface Flows. In: Kisler SF, Schweizer PM.Liquid Film Coating: Scientific principles and their technological implications. Chapman & Hall; 1997.
2. Schweizer PM. Visualization of coating flows. *J Fluid Mechanics*. 1988;193:285.
3. Sartor L. Slot Coating: Fluid Mechanics and Die Design. University of Minnesota. Published by University Microfilms International, Ann Arbor, MI. 1990. PhD Theses.
4. Chen K. Studies of Multilayer Slide Coating and Related Processes. University of Minnesota. Published by University Microfilms International, Ann Arbor, MI; 1992. PhD Theses.
5. Benjamin DF. Roll Coating Flows and Multiple Rolls Systems. University of Minnesota. Published by University Microfilms International, Ann Arbor, MI; 1994. PhD Theses.
6. Mues W, Hens J, Boiy L. Observation of a dynamic wetting process usig laser Doppler velocimetry. *AIChE J*. 1989;35(9):1521–1526.
7. Clarke A. The application of particle tracking velocimetry and flow visualisation to curtain coating. *Chem Eng Sci*. 1995;50(15):2397–2407.
8. Adrian R. Laser Velocimetry. In: Goldstein. Fluid Mechanics Measurements. Washington: Taylor and Francis; 1996.
9. Gomes BAA, Thompsom RL, Azevedo LFA. Solid Body Rotation Flow for Particle Image Velocimetry Calibration. 8th Brazilian Congress of Thermal Engineering and Science (ENCIT) 2000.
10. De Santos JM. Two-phase cocurrent down°ow through constricted passages. University of Minnesota; 1991. PhD Theses.
11. Bolstad JH, Keller HB. A multigrid continuation method for elliptic problems with folds. *SIAM J Scientific Stat Comput*. 1986;7(4):1081–1104.
12. Keller HB. Numerical solution of bifurcation and nonlinear eingenvalue problems. In: Rabinowitz PH. Applications of Bifurcation Theory. New York: Dekker; 1977.
13. Pearson JRA. The stability of uniform viscous flow under rollers and spreaders. *J Fluid Mech*. 1960;31:481–500.
14. Dontula P, Pasquali M, Scriven LE, Macosko CW. Model elastic liquids with water soluble polymers. *AIChE J*. 1998;44:1247–1255.
15. Rafael M, Willert C, Kompenhans J. Particle Image Velocimetry. A practical Guide. Berlin:Springer-Verla; 1998.


*Manuscript received Mar. 3, 2006, and revision received Sept. 26, 2006.*